Review Article

Pixel-Based Machine Learning in Medical Imaging

Kenji Suzuki

Department of Radiology, The University of Chicago, 5841 South Maryland Avenue, MC 2026, Chicago, IL 60637, USA

Correspondence should be addressed to Kenji Suzuki, suzuki@uchicago.edu

Machine learning (ML) plays an important role in the medical imaging field, including medical image analysis and computer-aided diagnosis, because objects such as lesions and organs may not be represented accurately by a simple equation; thus, medical pattern recognition essentially require "learning from examples." One of the most popular uses of ML is classification of objects such as lesions into certain classes (e.g., abnormal or normal, or lesions or nonlesions) based on input features (e.g., contrast and circularity) obtained from segmented object candidates. Recently, pixel/voxel-based ML (PML) emerged in medical image processing/analysis, which use pixel/voxel values in images directly instead of features calculated from segmented objects as input information; thus, feature calculation or segmentation is not required. Because the PML can avoid errors caused by inaccurate feature calculation and segmentation which often occur for subtle or complex objects, the performance of the PML can potentially be higher for such objects than that of common classifiers (i.e., feature-based MLs). In this paper, PMLs are surveyed to make clear (a) classes of PMLs, (b) similarities and differences within (among) different PMLs and those between PMLs and feature-based MLs, (c) advantages and limitations of PMLs, and (d) their applications in medical imaging.

1. Introduction

Machine learning (ML) plays an essential role in the medical imaging field, including medical image analysis and computer-aided diagnosis (CAD) [1, 2], because objects such as lesions and organs in medical images may be too complex to be represented accurately by a simple equation; modeling of such complex objects often requires a number of parameters which have to be determined by data. For example, a lung nodule is generally modeled as a solid sphere, but there are nodules of various shapes and nodules with internal inhomogeneities, such as spiculated nodules and ground-glass nodules [3]. A polyp in the colon is modeled as a bulbous object, but there are also polyps which exhibit a flat shape [4, 5]. Thus, diagnostic tasks in medical images essentially require "learning from examples (or data)" to determine a number of parameters in a complex model.

One of the most popular uses of ML in medical image analysis is the classification of objects such as lesions into certain classes (e.g., abnormal or normal, lesions or non-lesions, and malignant or benign) based on input features (e.g., contrast, area, and circularity) obtained from segmented

object candidates (This class of ML is referred to feature-based ML.). The task of ML here is to determine "optimal" boundaries for separating classes in the multidimensional feature space which is formed by the input features [6]. ML algorithms for classification include linear discriminant analysis [7], quadratic discriminant analysis [7], multilayer perceptron [8, 9], and support vector machines [10, 11]. Such ML algorithms were applied to lung nodule detection in chest radiography [12–15] and thoracic CT [16–19], classification of lung nodules into benign or malignant in chest radiography [20] and thoracic CT [21, 22], detection of microcalcifications in mammography [23–26], detection of masses in mammography [27], classification of masses into benign or malignant in mammography [28–30], polyp detection in CT colonography [31–33], determining subjective similarity measure of mammographic images [34–36], and detection of aneurysms in brain MRI [37].

Recently, as available computational power increased dramatically, pixel/voxel-based ML (PML) emerged in medical image processing/analysis which uses pixel/voxel values in images directly instead of features calculated from segmented regions as input information; thus, feature calculation or

TABLE 1: Classes of PMLs, their functions, and their applications.

PMLs	Functions	Applications
Neural filters (including neural edge enhancers)	Image processing	Edge-preserving noise reduction [38, 39]. Edge enhancement from noisy images [40]. Enhancement of subjective edges traced by a physician [41].
Convolution neural networks (including shift-invariant neural networks)	Classification	FP reduction in CAD for lung nodule detection in CXR [42–44]. FP reduction in CAD for detection of microcalcifications [45] and masses [46] in mammography. Face recognition [47]. Character recognition [48].
Massive-training artificial neural networks (MTANNs, including a mixture of expert MTANNs, a LAP-MTANN, an MTSVR)	Classification (image processing + scoring), pattern enhancement and suppression, object detection (pattern enhancement followed by thresholding or segmentation)	FP reduction in CAD for detection of lung nodules in CXR [57] and CT [17, 52, 63]. Distinction between benign and malignant lung nodules in CT [58]. FP reduction in CAD for polyp detection in CT colonography [53, 59–62]. Bone separation from soft tissue in CXR [54, 55]. Enhancement of lung nodules in CT [56].
Others	Image processing or classification	Segmenting posterior ribs in CXR [64]. Separation of ribs from soft tissue in CXR [65].

segmentation is not required. Because the PML can avoid errors caused by inaccurate feature calculation and segmentation which often occur for subtle or complex objects, the performance of the PML can potentially be higher for such objects than that of common classifiers (i.e., feature-based MLs). In this paper, PMLs are surveyed and reviewed to make clear (a) classes of PMLs, (b) the similarities and differences within different PMLs and those between PMLs and feature-based MLs, (c) the advantages and limitations of PMLs, and (d) their applications in medical imaging.

2. Pixel/Voxel-Based Machine Learning (PML)

2.1. Overview. PMLs have been developed for tasks in medical image processing/analysis and computer vision. Table 1 summarizes classes of PMLs, their functions, and their applications. There are three classes of PMLs: neural filters [38, 39] (including neural edge enhancers [40, 41]), convolution neural networks (NNs) [42–48] (including shift-invariant NNs [49–51]), and massive-training artificial neural networks (MTANNs) [52–56] (including multiple MTANNs [17, 38, 39, 52, 57, 58], a mixture of expert MTANNs [59, 60], a multiresolution MTANN [54], a Laplacian eigenfunction MTANN (LAP-MTANN) [61], and a massive-training support vector regression (MTSVR) [62]). The class of neural filters has been used for image-processing tasks such as edge-preserving noise reduction in radiographs and other digital pictures [38, 39], edge enhancement from noisy images [40], and enhancement of subjective edges traced by a physician in left ventriculograms [41]. The class of convolution NNs has been applied to classification tasks such as false-positive (FP) reduction in CAD schemes for detection of lung nodules in chest radiographs (also known as chest X-rays; CXRs) [42–44], FP reduction in CAD schemes for detection of microcalcifications [45] and masses [46] in mammography, face recognition [47], and character

recognition [48]. The class of MTANNs has been used for classification, such as FP reduction in CAD schemes for detection of lung nodules in CXR [57] and CT [17, 52, 63], distinction between benign and malignant lung nodules in CT [58], and FP reduction in a CAD scheme for polyp detection in CT colonography [53, 59–62]. The MTANNs have also been applied to pattern enhancement and suppression such as separation of bone from soft tissue in CXR [54, 55] and enhancement of lung nodules in CT [56]. There are other PML approaches in the literature. An iterative, pixel-based, supervised, statistical classification method called iterated contextual pixel classification has been proposed for segmenting posterior ribs in CXR [64]. A pixel-based, supervised regression filtering technique called filter learning has been proposed for separation of ribs from soft tissue in CXR [65].

2.2. Neural Filters. In the field of signal/image processing, supervised nonlinear filters based on a multilayer ANN, called neural filters, have been studied [38, 39]. The neural filter employs a linear-output ANN model as a convolution kernel of a filter. The inputs to the neural filter are an object pixel value and spatially/spatiotemporally adjacent pixel values in a subregion (or local window). The output of the neural filter is a single pixel value. The neural filter is trained with input images and corresponding "teaching" (desired or ideal) images. The training is performed by a linear-output backpropagation algorithm [40] which is a back-propagation algorithm modified for the linear-output ANN architecture. The input, output, and teacher (desired output) for neural filters are summarized in Table 2. Neural filters can acquire the functions of various linear and nonlinear filtering through training. Neural filters have been applied to reduction of the quantum noise in X-ray fluoroscopic and radiographic images [38, 39]. It was reported that the performance of the neural filter was superior to that of well-known nonlinear filters such as an adaptive weighted

TABLE 2: Classification of ML algorithms by their input, output, and teacher (desired output).

ML algorithms	Input	Output	Teacher
Neural filters	Pixel values in a subregion (local window) in a given image	Single pixel value (image is formed by collecting pixels)	Desired pixel value
MTANNs	Pixel values in a subregion (local window) in a given image	Single pixel value (image is formed by collecting pixels; likelihood score for the given image is obtained by use of the scoring method)	Likelihood of being a specific pattern at each pixel
Convolution NNs	Pixel values in a given image	Class to which the given image belongs	Nominal class label for the given image
Shift-invariant NNs	Pixel values in a given image	Class to which each pixel belongs	Nominal class label for each pixel
Multilayer perceptron for character recognition	Pixel values in a given binary image (character)	Class to which the given image belongs	Nominal class label for the given image
Classifiers (e.g., linear discriminant analysis, NNs, support vector machines)	Features extracted from a segmented object in a given image	Class to which the segmented object belongs	Nominal class label for the segmented object

averaging filter [66]. A study [38] showed that adding features from the subregion to the input information improved the performance of the neural filter. Neural filters have been extended to accommodate the task of enhancement of edges, and a supervised edge enhancer (detector), called a neural edge enhancer, was developed [40]. The neural edge enhancer can acquire the function of a desired edge enhancer through training. It was reported that the performance of the neural edge enhancer in the detection of edges from noisy images was far superior to that of well-known edge detectors such as the Canny edge detector [67], the Marr-Hildreth edge detector [68], and the Huckel edge detector [69]. In its application to the contour extraction of the left ventricular cavity in digital angiography, it has been reported that the neural edge enhancer can accurately replicate the subjective edges traced by a cardiologist [41].

2.3. Massive-Training Artificial Neural Network (MTANN). An MTANN was developed by extension of neural filters to accommodate various pattern-recognition tasks [52]. A two-dimensional (2D) MTANN was first developed for distinguishing a specific opacity (pattern) from other opacities (patterns) in 2D images [52]. The 2D MTANN was applied to reduction of FPs in computerized detection of lung nodules on 2D CT slices in a slice-by-slice way [17, 52, 63] and in CXR [57], the separation of ribs from soft tissue in CXR [54, 55, 70], and the distinction between benign and malignant lung nodules on 2D CT slices [58]. For processing of three-dimensional (3D) volume data, a 3D MTANN was developed by extending the structure of the 2D MTANN, and it was applied to 3D CT colonography data [53, 59–62].

The generalized architecture of an MTANN which unifies 2D and 3D MTANNs is shown in Figure 1. The input, output, and teacher for MTANNs are shown in Table 2. An MTANN consists of an ML model such as a linear-output ANN regression model and a support vector regression model, which is capable of operating on pixel/voxel data directly [40]. The linear-output ANN regression model employs a linear function instead of a sigmoid function as
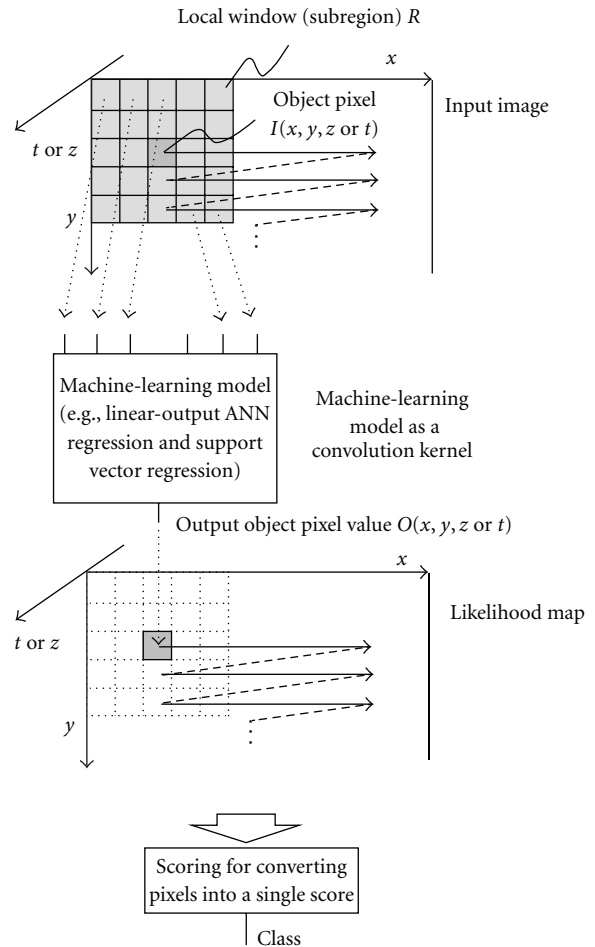

FIGURE 1: Generalized architecture of an MTANN (a class of PML) consisting of an ML model (e.g., linear-output ANN regression and support vector regression) with subregion input and single-pixel output. All pixel values in a subregion extracted from an input image are entered as input to the ML model. The ML model outputs a single pixel value for each subregion, the location of which corresponds to the center pixel in the subregion. Output pixel value is mapped back to the corresponding pixel in the output image.

the activation function of the unit in the output layer because the characteristics of an ANN were improved significantly with a linear function when applied to the continuous mapping of values in image processing [40]. Note that the activation functions of the units in the hidden layer are a sigmoid function for nonlinear processing, and those of the unit in the input layer are an identity function, as usual. The pixel/voxel values of the input images/volumes may be normalized from 0 to 1. The input to the MTANN consists of pixel/voxel values in a subregion/subvolume, R, extracted from an input image/volume. The output of the MTANN is a continuous scalar value, which is associated with the center voxel in the subregion, and is represented by

$$O(x, y, z \text{ or } t)$$
$$= \text{ML}\{I(x - i, y - j, z - k \text{ or } t - k) \mid (i, j, k) \in R\}, \tag{1}$$

where x, y, and z or t are the coordinate indices, $\text{ML}(\cdot)$ is the output of the ML model, and $I(x, y, z \text{ or } t)$ is a pixel/voxel value of the input image/volume. A three-layer structure may be selected as the structure of the ANN, because it has been proved that any continuous mapping can be approximated by a three-layer ANN [71, 72]. The structure of input units and the number of hidden units in the ANN may be designed by use of sensitivity-based unit-pruning methods [73, 74]. Other ML models such as support vector regression [10, 11] can be used as a core part of the MTANN. ML regression models rather than ML classification models would be suited for the MTANN framework, because the output of the MTANN is continuous scalar values (as opposed to nominal categories or classes). The entire output image/volume is obtained by scanning with the input subvolume of the MTANN on the entire input image/volume. The input subregion/subvolume and the scanning with the MTANN can be analogous to the kernel of a convolution filter and the convolutional operation of the filter, respectively.

The training of an MTANN is shown in Figure 2. The MTANN is trained with input images/volumes and the corresponding "teaching" images/volumes for enhancement of a specific pattern and suppression of other patterns in images/volumes. The "teaching" images/volumes are ideal or desired images for the corresponding input images/volumes. For enhancement of lesions and suppression of nonlesions, the teaching volume contains a map for the "likelihood of being lesions," represented by

$$T(x, y, z \text{ or } t) = \begin{cases} \text{a certain distribution,} & \text{for a lesion,} \\ 0, & \text{otherwise.} \end{cases} \tag{2}$$

To enrich the training samples, a training region, R_T, extracted from the input images is divided pixel by pixel into a large number of overlapping subregions. Single pixels are extracted from the corresponding teaching images as teaching values. The MTANN is massively trained by use of each of a large number of input subregions together with each of the corresponding teaching single pixels, hence the
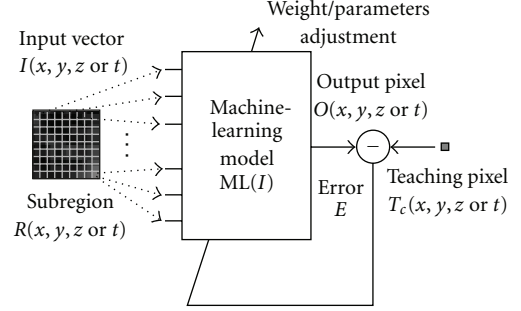

FIGURE 2: Training of an MTANN (a class of PML). An input vector is entered as input to the ML model. An error is calculated by subtracting of a teaching pixel from an output pixel. The parameters such as weights between layers in an ANN model are adjusted so that the error becomes small.

term "massive-training ANN." The error to be minimized by training of the MTANN is represented by

$$E = \frac{1}{P} \sum_c \sum_{(x,y,z \text{ or } t) \in R_T} \{T_c(x, y, z \text{ or } t) - O_c(x, y, z \text{ or } t)\}^2, \tag{3}$$

where c is a training case number, O_c is the output of the MTANN for the cth case, T_c is the teaching value for the MTANN for the cth case, and P is the number of total training voxels in the training region for the MTANN, R_T. The expert 3D MTANN is trained by a linear-output backpropagation (BP) algorithm [40] which was derived for the linear-output ANN model by use of the generalized delta rule [8]. After training, the MTANN is expected to output the highest value when a lesion is located at the center of the subregion of the MTANN, a lower value as the distance from the subregion center increases, and zero when the input subregion contains a nonlesion.

A scoring method is used for combining output pixels from the trained MTANNs. A score for a given region of interest (ROI) from the MTANN is defined as

$$S = \sum_{(x,y,z \text{ or } t) \in R_E} f_W(x, y, z \text{ or } t) \times O(x, y, z \text{ or } t), \tag{4}$$

where f_W is a weighting function for combining pixel-based output responses from the trained MTANN into a single score, which may often be the same distribution function used in the teaching images, and with its center corresponding to the center of the region for evaluation, R_E; and O is the output image of the trained MTANN, where its center corresponds to the center of R_E. This score represents the weighted sum of the estimates for the likelihood that the ROI (e.g., a lesion candidate) contains a lesion near the center; that is, a higher score would indicate a lesion and a lower score would indicate a non-lesion. Thresholding is then performed on the scores for distinction between lesions and non-lesions.

2.4. Convolution Neural Network (NN).

A convolution NN has first been proposed for handwritten ZIP-code recognition [75]. The architecture of a convolution NN is illustrated

in Figure 3. The input, output, and teacher for convolution NNs are summarized in Table 2. The convolution NN can be considered as a simplified version of the Neocognitron model [76–78] which was proposed to simulate the human visual system in 1980 [78]. The input and output of the convolution NN are images and nominal class labels, respectively. The convolution NN consists of one input layer, several hidden layers, and one output layer. The layers are connected with local shift-invariant interconnections (or convolution with a local kernel). Unlike the neocognitron, the convolution NN has no lateral interconnections or feedback loops, and the error BP algorithm [8] is used for training of the convolution NN. Units (neurons) in any hidden layer are organized in groups. Each unit in a subsequent layer is connected with the units of a small region in each group in the preceding layer. The groups between adjacent layers are interconnected by weights that are organized in kernels. For obtaining the shift-invariant responses, connection weights between any two groups in two layers are constrained to be shift-invariant; in other words, forward signal propagation is similar to a shift-invariant convolution operation. The signals from the units in a certain layer are convolved with the weight kernel, and the resulting value of the convolution is collected into the corresponding unit in the subsequent layer. This value is further processed by the unit through an activation function and produces an output signal. The activation function between two layers is a sigmoid function. For deriving the training algorithm for the convolution NN, the generalized delta rule [8] is applied to the architecture of the convolution NN. For distinguishing an ROI containing a lesion from an ROI containing a non-lesion, a class label (e.g., 1 for a lesion, 0 for a non-lesion) is assigned to an output unit.

Variants of the convolution NN have been proposed. The dual-kernel approach, which employs central kernels and peripheral kernels in each layer [43], was proposed for distinction between lung nodules and nonnodules in chest radiographs [42, 43] and distinction between microcalcifications and other anatomic structures in mammograms [43]. This dual-kernel-based convolution NN has several output units (instead of one or two output units in the standard convolution NN) for two-class classification. The fuzzy association was employed for transformation of output values from the output units to two classes (i.e., nodules or nonnodules; microcalcifications or other anatomic structures). A convolution NN which has subsampling layers has been developed for face recognition [47]. Some convolution NNs have one output unit [48, 79], some have two output units [80], and some have more than two output units [42, 43, 45, 47] for two-class classification.

Shift-invariant NNs [50, 51] are mostly the same as convolution NNs except for the output layer, which outputs images instead of classes. The shift-invariant NNs were used for localization (detection) of lesions in images, for example, detection of microcalcifications in mammograms [50, 51] and detection of the boundaries of the human corneal endothelium in photomicrographs [81].
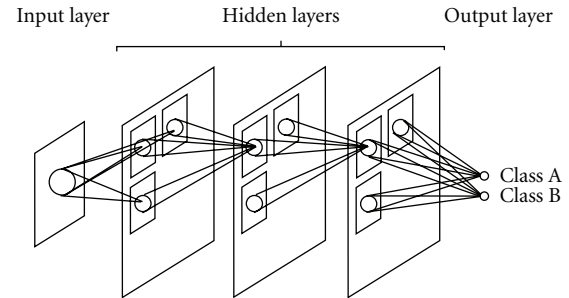

FIGURE 3: Architecture of a convolution NN (a class of PML). The convolution NN can be considered as a simplified version of the Neocognitron model, which was proposed to simulate the human visual system. The layers in the convolution NN are connected with local shift-invariant inter-connections (or convolution with a local kernel). The input and output of the convolution NN are images and nominal class labels (e.g., Class A and Class B), respectively.

2.5. Multilayer Perceptron for Character Recognition. A multilayer perceptron has been proposed for character recognition from an optical card reader [82, 83]. The architecture of the multilayer perceptron for character recognition is shown in Figure 4. The input, output, and teacher for the multilayer perceptron for character recognition are summarized in Table 2. The input and output of the multilayer perceptron are pixel values in a given binary image that contains a single character (e.g., a, b, or c) and a class to which the given image belongs, respectively. The number of input units equals the number of pixels in the given binary image (e.g., 16×16 pixels). The number of output units equals the number of classes (i.e., 26 for small-letter alphabetic characters). Each output unit is assigned to one of the classes. The class to which the given image belongs is determined as the class of the output unit with the maximum value. In the teaching data, a class label of 1 is assigned the corresponding output unit when a training sample belongs to that class; 0 is assigned to the other output units. Characters in given images are geometrically normalized before they are entered to the multilayer perceptron, because the architecture is not designed for being scale-invariant. Because character recognition with this type of the multilayer perceptron architecture is not shift-, rotation-, or scale-invariant, a large number of training samples is generally required. To enrich training samples, shifting, rotating, and scaling of training characters are often performed.

This type of multilayer perceptron has been applied to the classification of microcalcifications in mammography [23]. In this application, input images are not binary but gray-scale images. Pixel values in ROIs in mammograms or those in the Fourier-transformed ROIs were entered as input to the multilayer perceptron. In that study, the performance of the multilayer perceptrons based on ROIs in the spatial domain and the Fourier domain was found to be comparable.

2.6. Non-PML Feature-Based Classifiers. One of most popular uses of ML algorithms would probably be classification. In this use, an ML algorithm is called a classifier. A standard
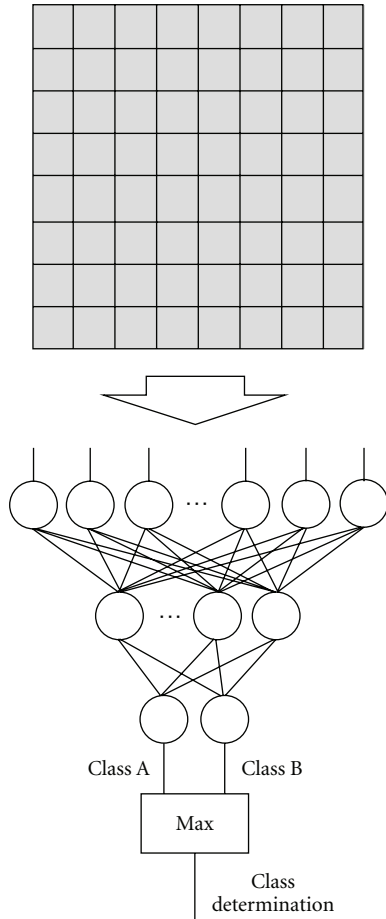
FIGURE 4: Architecture of a multilayer perceptron for character recognition. The binary pixel values in an image are entered as input to the multilayer perceptron. The class to which the given image belongs is determined as the class of the output unit with the maximum value.

classification approach based on a multilayer perceptron is illustrated in Figure 5. The input, output, and teacher for a classifier with features are summarized in Table 2. First, target objects are segmented by use of a segmentation method. Next, features are extracted from the segmented objects. Then, extracted features are entered as input to an ML model such as linear discriminant analysis [7], quadratic discriminant analysis [7], a multilayer perceptron [8, 9], and a support-vector machine [10, 11]. The ML model is trained with sets of input features and correct class labels. A class label of 1 is assigned to the corresponding output unit when a training sample belongs to that class, and 0 is assigned to the other output units. After training, the class of the unit with the maximum value is determined to be the corresponding class to which an unknown sample belongs. For details of feature-based classifiers, refer to one of many textbooks in pattern recognition such as [6–8, 10, 84].
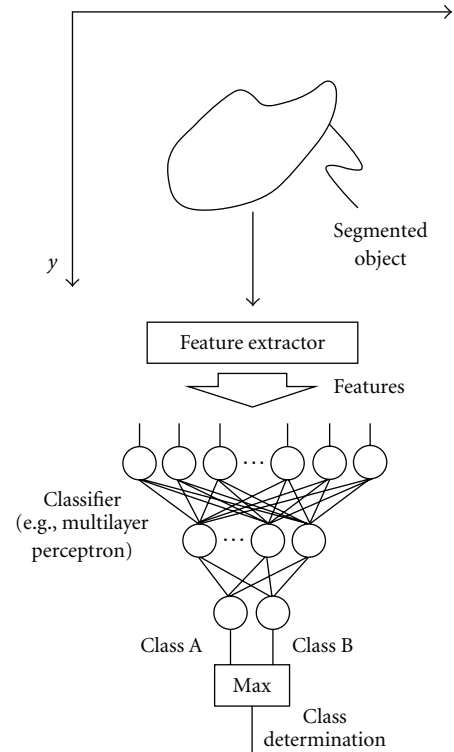

FIGURE 5: Standard classifier approach to classification of an object (i.e., feature-based ML). Features (e.g., contrast, effective diameter, and circularity) are extracted from a segmented object in an image. Those features are entered as input to a classifier such as a multilayer perceptron. Class determination is made by taking the class of the output unit with the maximum value.

3. Similarities and Differences

3.1. Within Different PML Algorithms. MTANNs [52] were developed by extension of neural filters to accommodate various pattern-recognition tasks. In other words, neural filters are a subclass or a special case of MTANNs. The applications and functions of neural filters are limited to noise reduction [38, 39] and edge enhancement [40, 41], whereas those of MTANNs were extended to include classification [52–54, 57–62], pattern enhancement and suppression [54], and object detection [56]. The input information to MTANNs, which is the pixel values in a subregion, is the same as that to neural filters. However, the output of (thus, teacher for) neural filters is the desired pixel values in a given image, whereas that of MTANNs is a map for the likelihood of being a specific pattern in a given image, as summarized in Table 2.

Both convolution NNs and the perceptron used for character recognition are in the class of PML. Input information to the convolution NNs and the perceptron is the pixel values in a given image, whereas the output of (thus, teacher for) both algorithms is a nominal class label for the given image. Thus, the input and output information are the same for both algorithms. However, the input images for the perceptron for character recognition are limited to be binary, although the perceptron itself is capable of processing

gray-scale images. The major difference between convolution NNs and the perceptron used for character recognition is their internal architectures. Units in layers of the perceptron are fully connected, whereas the connections in the convolution NN are spatially (locally) limited. Because of this architecture, forward signal propagation in the convolution NN is realized by a convolution operation. This convolution operation offers a shift-invariant property which is desirable for image classification. The applications and functions of the perceptron are limited to character recognition such as zip code recognition and optical character recognition, whereas those of convolution NNs are general classification of images into known classes such as classification of lesion candidates into lesions or nonlesions [42–46], classification of faces [47], and classification of characters [48].

Convolution NNs, shift-invariant NNs, and MTANNs perform convolution operations. In convolution NNs and shift-invariant NNs, convolution operations are performed within the network, as shown in Figure 3, whereas the convolutional operation is performed outside the network in the MTANN, as shown in Figure 1.

3.2. Between PML Algorithms and Ordinary Classifiers.

The major difference between PMLs and ordinary classifiers (i.e., feature-based classifiers) is the input information. Ordinary classifiers use features extracted from a segmented object in a given image, whereas PMLs use pixel values in a given image as the input information. Although the input information to PMLs can be features (see addition of features to the input information to neural filters in [38], i.e.), these features are obtained pixel by pixel (rather than by object). In other words, features for PMLs are features at each pixel in a given image, whereas features for ordinary classifiers are features from a segmented object. In that sense, feature-based classifiers may be referred to as object-based classifiers. Because PMLs use pixel/voxel values in images directly instead of features calculated from segmented objects as the input information, feature calculation or segmentation is not required. Although the development of segmentation techniques has been studied for a long time, segmentation of objects is still challenging, especially for complicated objects, subtle objects, and objects in a complex background. Thus, segmentation errors may occur for complicated objects. Because, with PMLs, errors caused by inaccurate feature calculation and segmentation can be avoided, the performance of PMLs can be higher than that of ordinary classifiers for some cases, such as complicated objects.

The output information from ordinary classifiers, convolution NNs, and the perceptron used for character recognition is nominal class labels, whereas that from neural filters, MTANNs, and shift-invariant NNs is images. With the scoring method in MTANNs, output images of the MTANNs are converted to likelihood scores for distinguishing among classes, which allow MTANNs to do classification. In addition to classification, MTANNs can perform pattern enhancement and suppression as well as object detection, whereas the other PMLs cannot.

4. Applications of PML Algorithms in Medical Images

4.1. Edge-Preserving Noise Reduction by Use of Neural Filters.

Quantum noise is dominant in low-radiation-dose X-ray images used in diagnosis. For training a neural filter to reduce quantum noise in diagnostic X-ray images while preserving image details such as edges, noisy input images and corresponding "teaching" images are necessary. When a high radiation dose is used, X-ray images with little noise can be acquired and used as the "teaching" images. A noisy input image can be synthesized by addition of simulated quantum noise (which is modeled as signal-dependent noise) to a noiseless original high-radiation-dose image $f_o(x, y)$, represented by

$$f_N(x, y) = f_o(x, y) + n[\sigma\{f_o(x, y)\}], \qquad (5)$$

where $n[\sigma\{f_o(x, y)\}]$ is noise with standard deviation $\sigma\{f_o(x, y)\} = k_N\sqrt{f_o(x, y)}$ and k_N is a parameter determining the amount of noise. A synthesized noisy X-ray image obtained with this method and a noiseless original high-radiation-dose X-ray image are illustrated in Figure 6(a). They are angiograms of coronary arteries. They were used as the input image and as the teaching image for training of a neural filter. For sufficient reduction of noise, the input region of the neural filter consisted of 11×11 pixels. For efficient training of the entire image, 5,000 training pixels were sampled randomly from the input and teaching images. The training of the neural filter was performed for 100,000 iterations. The output image of the trained neural filter for a nontraining case is shown in Figure 6(b). The noise in the input image is reduced while image details such as the edges of arteries are maintained. When an averaging filter was used for noise reduction, the edges of arteries were blurry, as shown in Figure 6(b).

4.2. Edge Enhancement from Noisy Images by Use of Neural Edge Enhancer.

Although conventional edge enhancers can very well enhance edges in images with little noise, they do not work well on noisy images. To address this issue, a neural edge enhancer has been developed for enhancing edges from very noisy images [40]. The neural edge enhancer is based on a neural filter and can be trained with input images and corresponding "teaching" edge images. Figure 7(a) shows a way of creating noisy input images and corresponding "teaching" edge images from a noiseless image for training of a neural edge enhancer. Simulated quantum noise was added to original noiseless images to create noisy input images. A Sobel edge enhancer [85] was applied to the original noiseless images to create "teaching" edge images. The key here is that the Sobel edge enhancer works very well for noiseless images. The neural edge enhancer was trained with the noisy input images together with the corresponding teaching edge images. For comparison, the trained neural edge enhancer and the Sobel edge enhancer were applied to nontraining noisy images. The resulting nontraining edge-enhanced images are shown in Figure 7(b). Edges are enhanced clearly in the output image of the neural edge
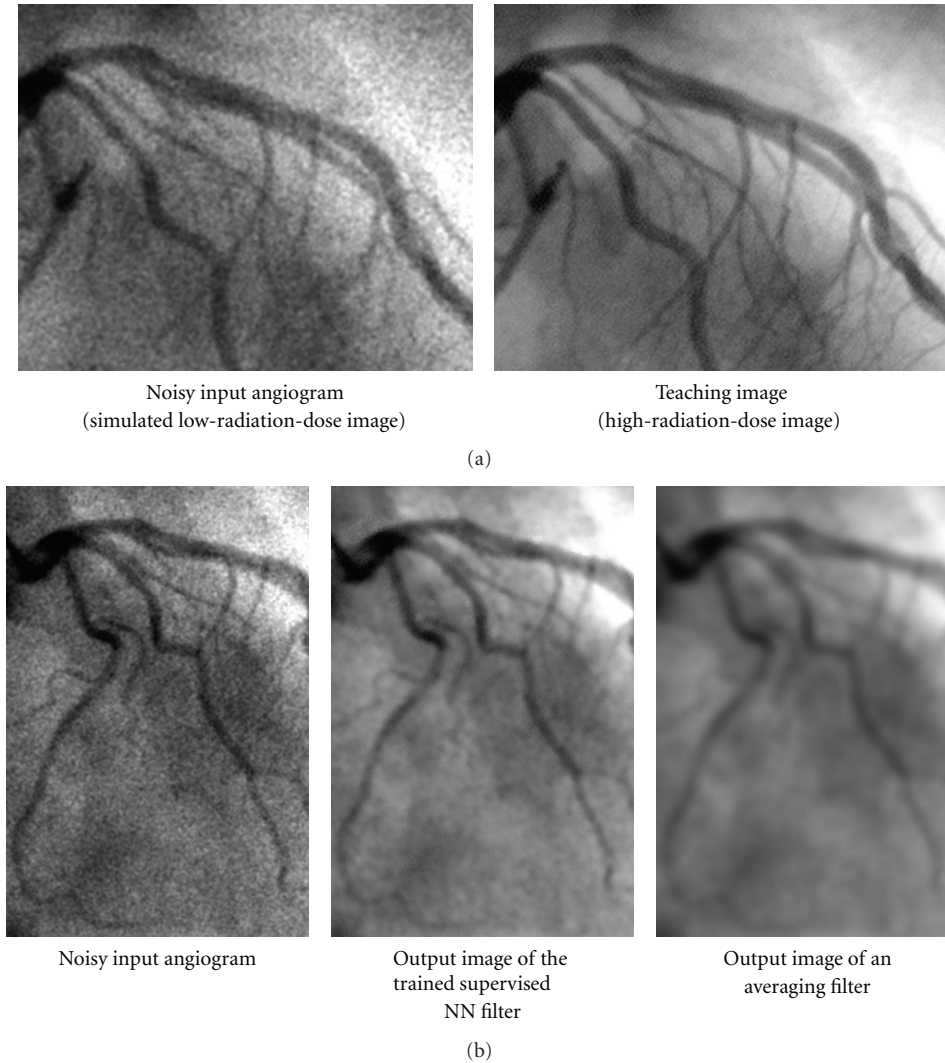
Noisy input angiogram
(simulated low-radiation-dose image)

Teaching image
(high-radiation-dose image)

(a)

Noisy input angiogram

Output image of the
trained supervised
NN filter

Output image of an
averaging filter

(b)

FIGURE 6: Reduction of quantum noise in angiograms by using a supervised NN filter called a "neural filter." (a) Images used for training of the neural filter. (b) Result of an application of the trained neural filter to a nontraining image and a comparison result with an averaging filter.

enhancer while noise is suppressed, whereas the Sobel edge enhancer enhances not only edges but also noise.

4.3. Bone Separation from Soft Tissue in Chest Radiographs (CXRs) by Use of MTANNs. CXR is the most frequently used diagnostic imaging examination for chest diseases such as lung cancer, tuberculosis, and pneumonia. More than 9 million people worldwide die annually from chest diseases [86]. Lung cancer causes 945,000 deaths and is the leading cause of cancer deaths in the world [86] and in countries such as the United States, the United Kingdom, and Japan [87]. Lung nodules (i.e., potential lung cancers) in CXR, however, can be overlooked by radiologists in from 12 to 90% of cases that have nodules visible in retrospect [88, 89]. Studies showed that 82 to 95% of the missed lung cancers were partly obscured by overlying bones such as ribs and/or a clavicle [88, 89]. To address this issue, dual-energy imaging has been

investigated [90, 91]. Dual-energy imaging uses the energy dependence of the X-ray attenuation by different materials; it can produce two tissue-selective images, that is, a "bone" image and a "soft-tissue" image [92–94]. Major drawbacks of dual-energy imaging, however, are that (a) the radiation dose can be double, (b) specialized equipment for obtaining dual-energy X-ray exposures is required, and (c) the subtraction of two-energy images causes an increased noise level in the images.

For resolving the above drawbacks with dual-energy images, MTANNs have been developed as an image-processing technique for separation of ribs from soft tissue [54, 70]. The basic idea is to train the MTANN with soft-tissue and bone images acquired with a dual-energy radiography system [92, 95, 96]. For separation of ribs from soft tissue, the MTANN was trained with input CXRs and the corresponding "teaching" dual-energy bone images, as illustrated in **Figure 8(a)**. **Figure 8(b)** shows a nontraining

High-radiation-dose angiogram

Adding noise   Sobel edge enhancer

Noisy angiogram   Edge-enhanced image

(a)

Noisy input angiogram   Output image of the trained neural edge enhancer   Output image of the Sobel edge enhancer
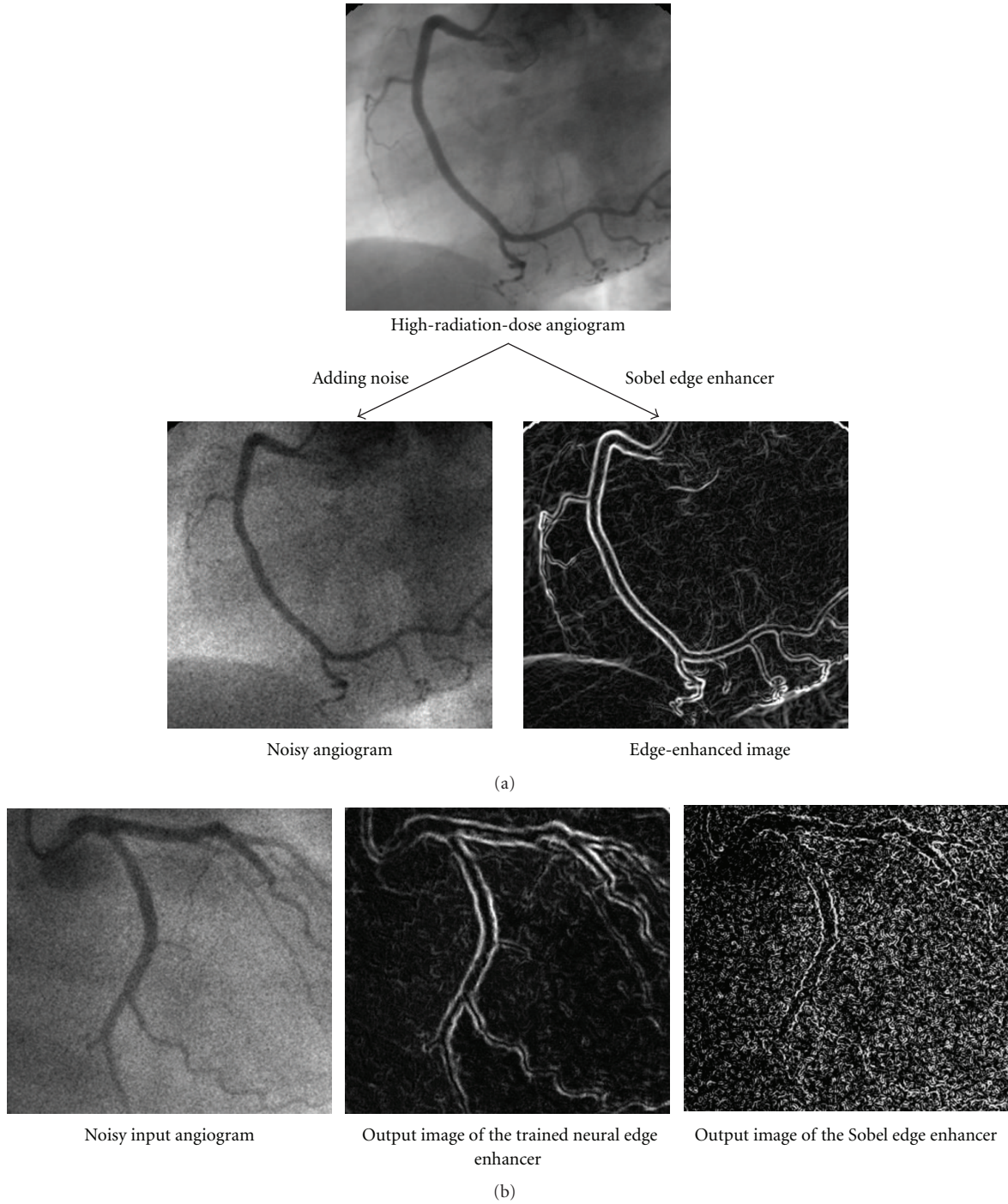
(b)

FIGURE 7: Enhancement of edges from noisy images by use of a supervised edge enhancer called a "neural edge enhancer." (a) A way to create noisy input images and corresponding "teaching" edge images from noiseless images for training a neural edge enhancer. (b) Result of an application of the trained neural edge enhancer to a nontraining image and a comparison result with a Sobel edge enhancer.

original CXR and a soft-tissue image obtained by use of the trained MTANN. The contrast of ribs is suppressed substantially in the MTANN soft-tissue image, whereas the contrast of soft tissue such as lung vessels is maintained. There is another PML approach called filter learning to do the same task [64].

4.4. Enhancement and Detection of Lesions by Use of MTANNs. Computer-aided diagnosis (CAD) has been an active area of study in medical image analysis [1, 2, 97, 98]. Some CAD schemes employ a filter for enhancement of lesions as a preprocessing step for improving sensitivity and specificity, but some do not employ such a filter. The filter enhances

Input chest radiograph   "Teaching" dual-energy soft-tissue image

(a)

Original chest radiograph   Soft-tissue image by the trained MTANN
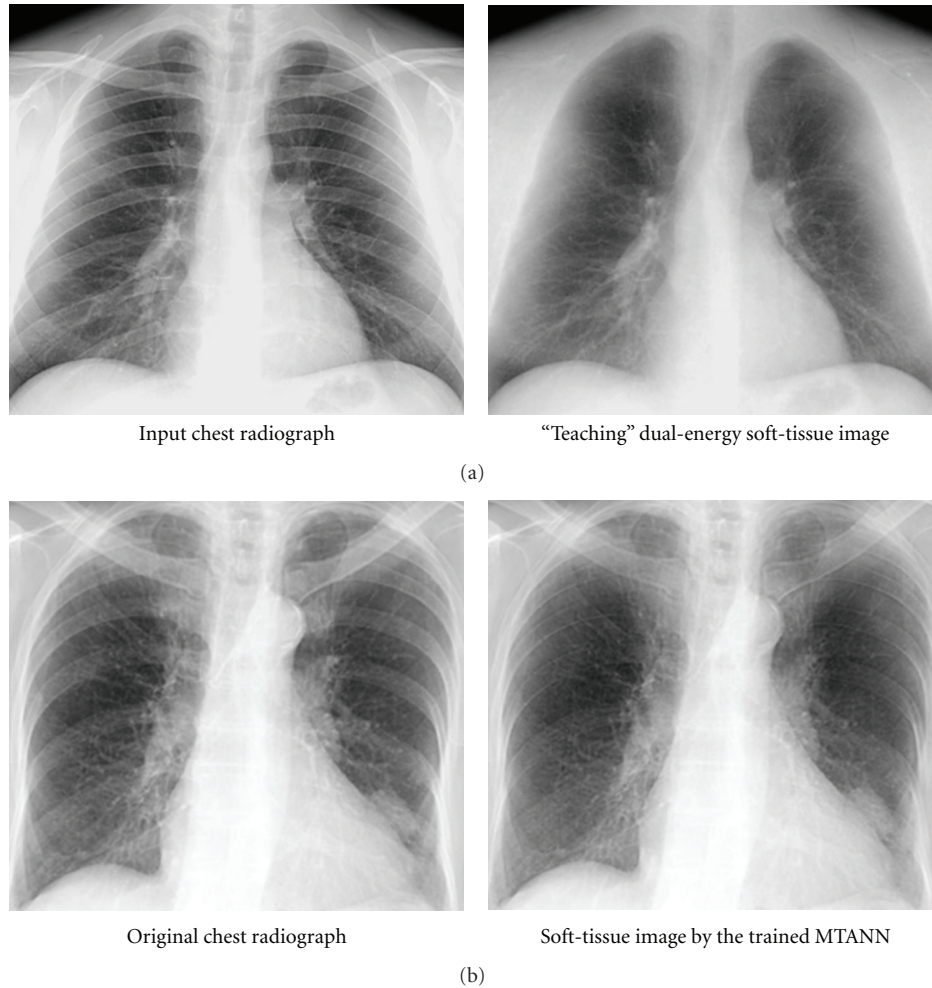
(b)

FIGURE 8: Separation of bones from soft tissue in CXRs by use of an MTANN. (a) Images used for training the MTANN. (b) Result of an application of the trained MTANN to a nontraining CXR.

objects similar to a model employed in the filter; for example, a blob-enhancement filter based on the Hessian matrix enhances sphere-like objects [99]. Actual lesions, however, often differ from a simple model; for example, a lung nodule is generally modeled as a solid sphere, but there are nodules of various shapes and inhomogeneous nodules such as nodules with spiculation and ground-glass nodules. Thus, conventional filters often fail to enhance such actual lesions.

To address this issue, a "lesion-enhancement" filter based on MTANNs has been developed for enhancement of actual lesions in a CAD scheme for detection of lung nodules in CT [56]. For enhancement of lesions and suppression of non-lesions in CT images, the teaching image contains a map for the "likelihood of being lesions." For enhancement of a nodule in an input CT image, a 2D Gaussian distribution was placed at the location of the nodule in the teaching image, as a model of the likelihood of being a lesion. For testing of the performance, the trained MTANN was applied to nontraining lung CT images. As shown in Figure 9, the nodule is enhanced in the output image of the trained MTANN filter, while normal structures such as lung vessels

are suppressed. Note that small remaining regions due to vessels can easily be separated from nodules by use of their area information which can be obtained by use of connected-component labeling [100–102].

4.5. Classification between Lesions and Nonlesions by Use of Different PML Algorithms

4.5.1. MTANNs. Shift-invariant NNs are mostly the same as convolution NNs except for the output layer, which outputs images instead of classes. The shift-invariant NNs can be used for localization (detection) of objects in images in addition to classification [50, 51]. A major challenge in CAD development is to reduce the number of FPs [27, 103–107], because there are various normal structures similar to lesions in medical images. To address this issue, an FP-reduction technique based on an MTANN has been developed for a CAD scheme for lung nodule detection in CT [52]. For enhancement of nodules (i.e., true positives) and suppression of nonnodules (i.e., FPs) on CT images, the teaching

Input chest CT image
with a nodule (arrow)

(a)

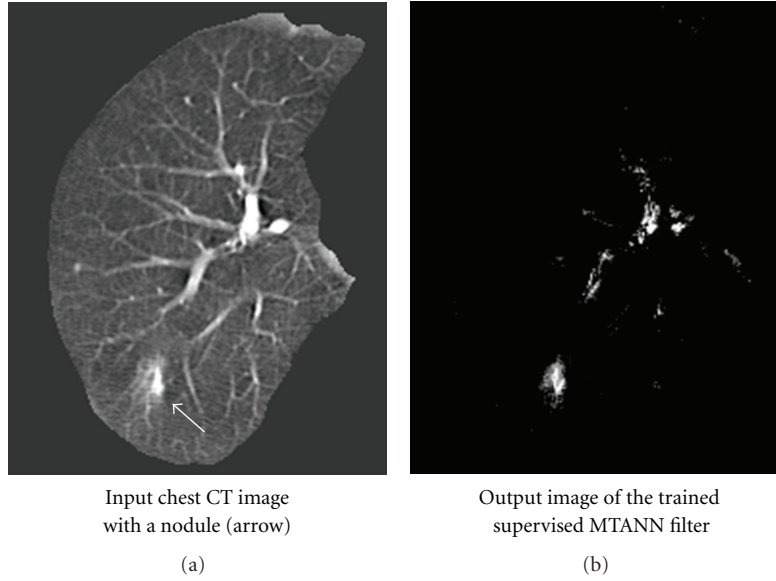Output image of the trained
supervised MTANN filter

(b)

FIGURE 9: Enhancement of a lesion by use of the trained lesion-enhancement MTANN filter for a nontraining case. (a) Original chest CT image of the segmented lung with a nodule (indicated by an arrow). (b) Output image of the trained lesion-enhancement MTANN filter.
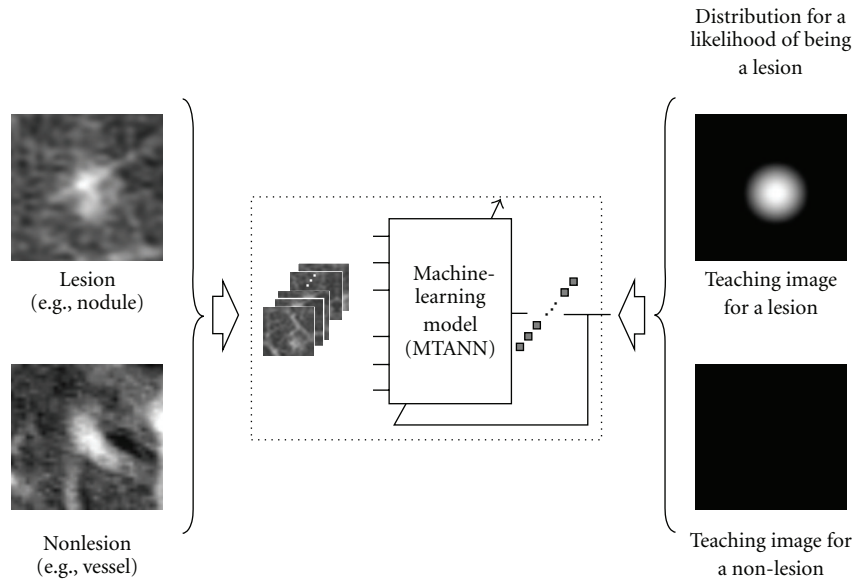

Distribution for a
likelihood of being
a lesion

Lesion
(e.g., nodule)

Machine-
learning
model
(MTANN)

Teaching image
for a lesion

Nonlesion
(e.g., vessel)

Teaching image for
a non-lesion

FIGURE 10: Training of an MTANN for distinction between lesions and non-lesions in a CAD scheme for detection of lesions in medical images. The teaching image for a lesion contains a Gaussian distribution; that for a non-lesion contains zero (completely dark). After the training, the MTANN expects to enhance lesions and suppress non-lesions.

image contains a distribution of values that represent the "likelihood of being a nodule." For example, the teaching volume contains a 3D Gaussian distribution with standard deviation σ_T for a lesion and zero (i.e., completely dark) for non-lesions, as illustrated in Figure 10. This distribution represents the "likelihood of being a lesion":

$$
T(x, y, z \text{ or } t)
$$
$$
= \begin{cases} \dfrac{1}{\sqrt{2\pi}\sigma_T} \ \exp\left\{ -\dfrac{(x^2 + y^2 + z^2 \text{ or } t^2)}{2\sigma_T^2} \right\}, & \text{for a lesion,} \\ 0, & \text{otherwise.} \end{cases}
$$
$$
(6)
$$

A 3D Gaussian distribution is used to approximate an average shape of lesions. The MTANN involves training with a large number of subvolume-voxel pairs, which is called a massive-subvolumes training scheme.

A scoring method is used for combining of output voxels from the trained MTANNs, as illustrated in Figure 11. A score for a given ROI from the MTANN is defined as

$$
S = \sum_{(x,y,z \text{ or } t) \in R_E} f_W(x, y, z \text{ or } t) \times O(x, y, z \text{ or } t), \qquad (7)
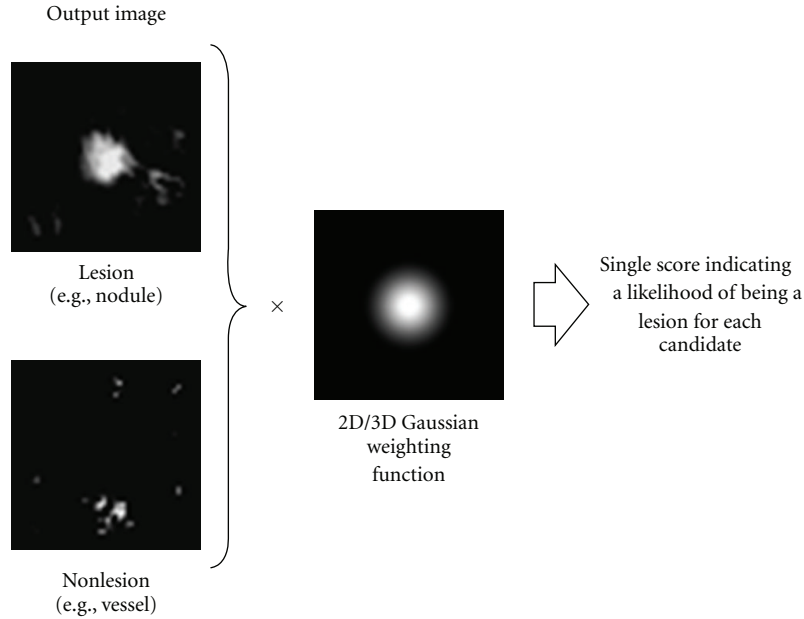$$

Figure 11: Scoring method for combining pixel-based output responses from the trained MTANN into a single score for each ROI.

where

$$f_W(x, y, z \text{ or } t)$$
$$= f_G(x, y, z \text{ or } t; \sigma) = \frac{1}{\sqrt{2\pi}\sigma} e^{-(x^2+y^2+z^2 \text{ or } t^2)/2\sigma^2} \quad (8)$$

is a 3D Gaussian weighting function with standard deviation σ and with its center corresponding to the center of the volume for evaluation, R_E, and O is the output image of the trained MTANN, where its center corresponds to the center of R_E. The use of the 3D Gaussian weighting function allows us to combine the responses (outputs) of a trained MTANN as a 3D distribution. A 3D Gaussian function is used for scoring, because the output of a trained MTANN is expected to be similar to the 3D Gaussian distribution used in the teaching images. This score represents the weighted sum of the estimates for the likelihood that the ROI (lesion candidate) contains a lesion near the center; that is, a higher score would indicate a lesion and a lower score would indicate a nonlesion. Thresholding is then performed on the scores for distinction between lesions and non-lesions.

An MTANN was trained with typical nodules and typical types of FPs (nonnodules) and corresponding teaching images. The trained MTANN was applied to 57 true positives (nodules) and 1,726 FPs (nonnodules) produced by a CAD scheme [52]. Figure 12 shows various types of nodules and nonnodules and the corresponding output images of the trained MTANN. Nodules such as a solid nodule, a part-solid (mixed-ground-glass) nodule, and a non-solid (ground-glass) nodule are enhanced, whereas nonnodules such as different-sized lung vessels and soft-tissue opacity are suppressed around the centers of ROIs. For combining output pixels into a single score for each nodule candidate, a scoring method was applied to the output images for distinction between a nodules and a nonnodule. Thresholding of

scores was done for classification of nodule candidates into nodules or nonnodules. Free-response receiver operating characteristic (FROC) analysis [108] was carried out for evaluation of the performance of the trained MTANN. The FROC curve for the MTANN indicates 80.3% overall sensitivity (100% classification performance) and a reduction in the FP rate from 0.98 to 0.18 per section, as shown in Figure 13.

4.5.2. Convolution NNs and Shift-Invariant NNs.
Convolution NNs have been used for FP reduction in CAD schemes for lung nodule detection in CXRs [42–44]. A convolution NN was trained with 28 chest radiographs for distinguishing lung nodules from nonnodules (i.e., FPs produced by an initial CAD scheme). The trained convolution NN reduced 79% of FP detections (which is equivalent to 2-3 FPs per patient), while 80% of true-positive detections were preserved. Convolution NNs have been applied to FP reduction in CAD schemes for detection of microcalcifications [45] and masses [46] in mammography. A convolution NN was trained with 34 mammograms for distinguishing microcalcifications from FPs. The trained convolution NN reduced 90% of FP detections, which resulted in 0.5 FP detections per image, while a true-positive detection rate of 87% was preserved [45].

Shift-invariant NNs have been used for FP reduction in CAD for detection of microcalcifications [50, 51]. A shift-invariant NN was trained to detect microcalcifications in ROIs. Microcalcifications were detected by thresholding of the output images of the trained shift-invariant NN. When the number of detected microcalcifications was greater than a predetermined number, the ROI was considered as a microcalcification ROI. With the trained shift-invariant NN, 55% of FPs was removed without any loss of true positives.
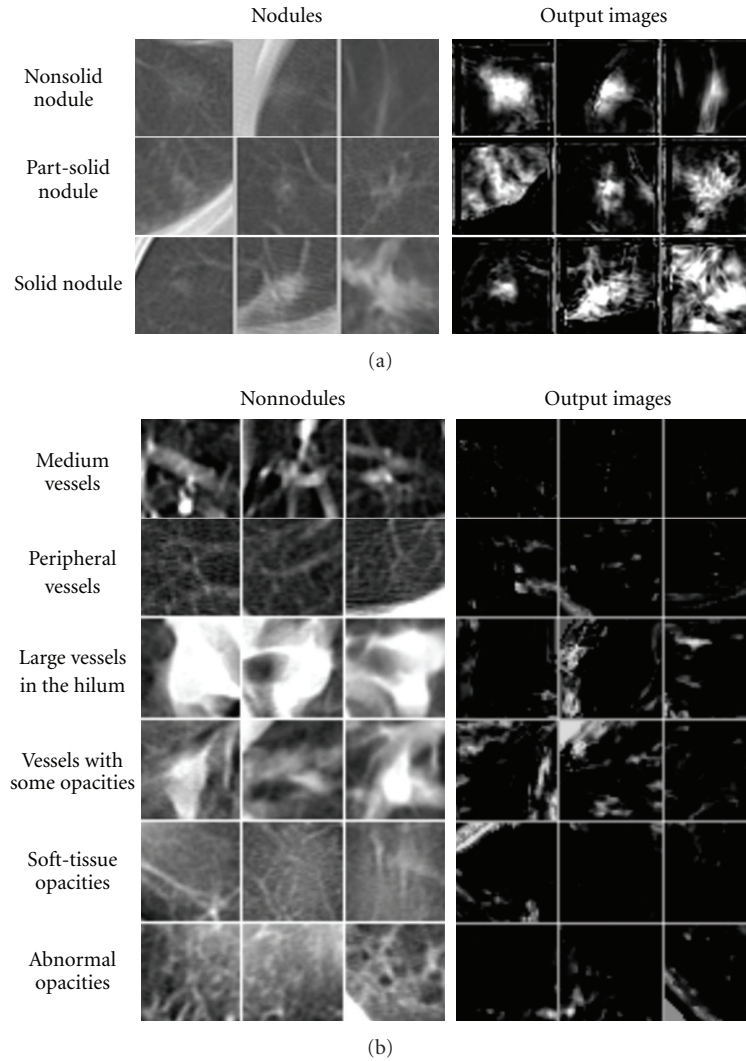
(a)

(b)

FIGURE 12: Illustrations of various types of nontraining nodules and nonnodules and corresponding output images of the trained MTANN. Nodules are represented by bright pixels, whereas nonnodules are almost dark around the centers of ROIs.

5. Advantages and Limitations of PML Algorithms

As described earlier, the major difference between PMLs and ordinary classifiers is the direct use of pixel values with PML. In other words, unlike ordinary classifiers, feature calculation from segmented objects is not necessary. Because the PML can avoid errors caused by inaccurate feature calculation and segmentation, the performance of the PML can potentially be higher than that of ordinary feature-based classifiers for some cases. PMLs learn pixel data directly, and thus all information on pixels should not be lost before the pixel data are entered into the PML, whereas ordinary feature-based classifiers learn the features extracted from segmented lesions and thus important information can be lost with this indirect extraction; also, inaccurate segmentation often occurs for complicated patterns. In addition, because feature calculation is not required for PML, development and implementation of segmentation and feature calculation, and selection of features are unnecessary.

Ordinary classifiers such as linear discriminant analysis, ANNs, and support vector machines cannot be used for image processing, detection (localization) of objects, or enhancement of objects or patterns, whereas MTANNs can do those tasks. For example, MTANNs can separate bones from soft tissue in CXRs [54], and MTANN can enhance and detect lung nodules on CT images [56].

The characteristics of PMLs which use pixel data directly should differ from those of ordinary feature-based classifiers. Therefore, combining an ordinary feature-based classifier with a PML would yield a higher performance than that of a classifier alone or a PML alone. Indeed, in previous studies, both classifier and PML were used successfully for classification of lesion candidates into lesions and non-lesions [17, 45, 46, 49–53, 58–63].

A limitation of PMLs is the relatively long time for training because of the high dimensionality of input data. Because
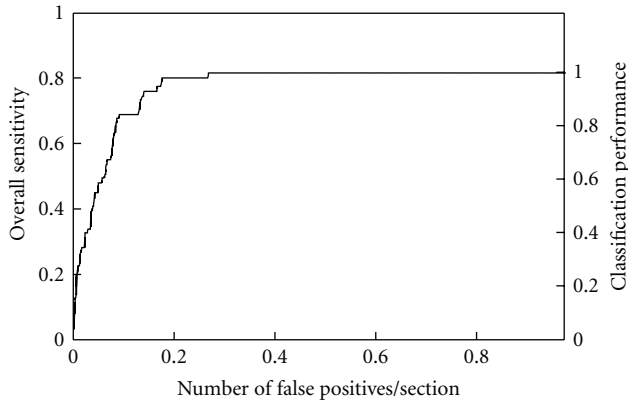
FIGURE 13: FROC curve indicating the performance of the MTANN in distinction between 57 true positives (nodules) and 1.726 FPs (nonnodules).

PMLs use pixel data in images directly, the number of input dimensions is generally large. For example, a 3D MTANN for 3D CT data requires 171 dimensions for its input [53, 60]. The ordinary feature-based classifiers are more efficient than PMLs. In an application of PMLs and feature-based classifiers to CAD schemes, a feature-based classifier should be applied first, because the number of lesion candidates that need to be classified is larger at an earlier stage. After the number of lesion candidates is reduced by use of the feature-based classifier, a PML should be applied for further reduction of FPs. Indeed, previous studies employed this strategy [17, 52, 53, 58–61].

To address the issue of training time for PML, dimensionality reduction methods for PML have been proposed [61]. With the use of the Laplacian-eigenfunction-based dimensionality reduction of the input vectors to a 3D MTANN, the training time was reduced by a factor of 8.5.

6. Conclusion

In this paper, PMLs were surveyed and compared with each other as well as with other non-PML algorithms (i.e., ordinary feature-based classifiers) to make the similarities, differences, advantages, and limitations clear. The major difference between PMLs and non-PML algorithms (e.g., classifiers) is a need for segmentation and feature calculation with non-PML algorithms. The major advantage of PMLs over non-PML algorithms is that no information is lost due to inaccurate segmentation and feature calculation, which would result in a higher performance for some cases such as complicated patterns. With the combination of PMLs with non-PML algorithms, the performance of a system can be improved substantially. In addition to a classification task, MTANNs can be used for enhancement (and suppression) and detection (i.e., localization) of objects (or patterns) in images.

References

[1] M. L. Giger and K. Suzuki, "Computer-aided diagnosis (CAD)," in *Biomedical Information Technology*, D. D. Feng, Ed., pp. 359–374, Academic Press, New York, NY, USA, 2007.

[2] K. Doi, "Current status and future potential of computer-aided diagnosis in medical imaging," *British Journal of Radiology*, vol. 78, supplement 1, pp. S3–S19, 2005.

[3] F. Li, S. Sone, H. Abe, H. MacMahon, S. G. Armato III, and K. Doi, "Lung cancers missed at low-dose helical CT screening in a general population: comparison of clinical, histopathologic, and imaging findings," *Radiology*, vol. 225, no. 3, pp. 673–683, 2002.

[4] A. Lostumbo, C. Wanamaker, J. Tsai, K. Suzuki, and A. H. Dachman, "Comparison of 2D and 3D views for evaluation of flat lesions in CT colonography," *Academic Radiology*, vol. 17, no. 1, pp. 39–47, 2010.

[5] R. M. Soetikno, T. Kaltenbach, R. V. Rouse et al., "Prevalence of nonpolypoid (flat and depressed) colorectal neoplasms in asymptomatic and symptomatic adults," *Journal of the American Medical Association*, vol. 299, no. 9, pp. 1027–1035, 2008.

[6] R. O. Duda, P. E. Hart, and D. G. Stork, in *Pattern Recognition*, Wiley Interscience, Hoboken, NJ, USA, 2nd edition, 2001.

[7] K. Fukunaga, *Introduction to Statistical Pattern Recognition*, Academic Press, San Diego, Calif, USA, 2nd edition, 1990.

[8] D. E. Rumelhart, G. E. Hinton, and R. J. Williams, "Learning representations by back-propagating errors," *Nature*, vol. 323, no. 6088, pp. 533–536, 1986.

[9] D. E. Rumelhart, G. E. Hinton, and R. J. Williams, "Learning internal representations by error propagation," *Parallel Distributed Processing*, vol. 1, pp. 318–362, 1986.

[10] V. N. Vapnik, *The Nature of Statistical Learning Theory*, Springer-Verlag, Berlin, Germany, 1995.

[11] V. N. Vapnik, *Statistical Learning Theory*, Wiley, New York, NY, USA, 1998.

[12] J. Shiraishi, Q. Li, K. Suzuki, R. Engelmann, and K. Doi, "Computer-aided diagnostic scheme for the detection of lung nodules on chest radiographs: localized search method based

on anatomical classification," *Medical Physics*, vol. 33, no. 7, pp. 2642–2653, 2006.

[13] G. Coppini, S. Diciotti, M. Falchini, N. Villari, and G. Valli, "Neural networks for computer-aided diagnosis: detection of lung nodules in chest radiograms," *IEEE Transactions on Information Technology in Biomedicine*, vol. 7, no. 4, pp. 344–357, 2003.

[14] R. C. Hardie, S. K. Rogers, T. Wilson, and A. Rogers, "Performance analysis of a new computer aided detection system for identifying lung nodules on chest radiographs," *Medical Image Analysis*, vol. 12, no. 3, pp. 240–258, 2008.

[15] S. Chen, K. Suzuki, and H. MacMahon, "Development and evaluation of a computer-aided diagnostic scheme for lung nodule detection in chest radiographs by means of two-stage nodule enhancement with support vector classification," *Medical Physics*, vol. 38, no. 4, pp. 1844–1858, 2011.

[16] S. G. Armato III, M. L. Giger, and H. MacMahon, "Automated detection of lung nodules in CT scans: preliminary results," *Medical Physics*, vol. 28, no. 8, pp. 1552–1561, 2001.

[17] H. Arimura, S. Katsuragawa, K. Suzuki et al., "Computerized scheme for automated detection of lung nodules in low-dose computed tomography images for lung cancer screening," *Academic Radiology*, vol. 11, no. 6, pp. 617–629, 2004.

[18] X. Ye, X. Lin, J. Dehmeshki, G. Slabaugh, and G. Beddoe, "Shape-based computer-aided detection of lung nodules in thoracic CT images," *IEEE Transactions on Biomedical Engineering*, vol. 56, no. 7, Article ID 5073252, pp. 1810–1820, 2009.

[19] T. W. Way, B. Sahiner, H. P. Chan et al., "Computer-aided diagnosis of pulmonary nodules on CT scans: improvement of classification performance with nodule surface features," *Medical Physics*, vol. 36, no. 7, pp. 3086–3098, 2009.

[20] M. Aoyama, Q. Li, S. Katsuragawa, H. MacMahon, and K. Doi, "Automated computerized scheme for distinction between benign and malignant solitary pulmonary nodules on chest images," *Medical Physics*, vol. 29, no. 5, pp. 701–708, 2002.

[21] M. Aoyama, Q. Li, S. Katsuragawa, F. Li, S. Sone, and K. Doi, "Computerized scheme for determination of the likelihood measure of malignancy for pulmonary nodules on low-dose CT images," *Medical Physics*, vol. 30, no. 3, pp. 387–394, 2003.

[22] S. K. Shah, M. F. McNitt-Gray, S. R. Rogers et al., "Computer aided characterization of the solitary pulmonary nodule using volumetric and contrast enhancement features," *Academic Radiology*, vol. 12, no. 10, pp. 1310–1319, 2005.

[23] Y. Wu, K. Doi, M. L. Giger, and R. M. Nishikawa, "Computerized detection of clustered microcalcifications in digital mammograms: applications of artificial neural networks," *Medical Physics*, vol. 19, no. 3, pp. 555–560, 1992.

[24] I. El-Naqa, Y. Yang, M. N. Wernick, N. P. Galatsanos, and R. M. Nishikawa, "A support vector machine approach for detection of microcalcifications," *IEEE Transactions on Medical Imaging*, vol. 21, no. 12, pp. 1552–1563, 2002.

[25] S. N. Yu, K. Y. Li, and Y. K. Huang, "Detection of microcalcifications in digital mammograms using wavelet filter and Markov random field model," *Computerized Medical Imaging and Graphics*, vol. 30, no. 3, pp. 163–173, 2006.

[26] J. Ge, B. Sahiner, L. M. Hadjiiski et al., "Computer aided detection of clusters of microcalcifications on full field digital mammograms," *Medical Physics*, vol. 33, no. 8, pp. 2975–2988, 2006.

[27] Y. T. Wu, J. Wei, L. M. Hadjiiski et al., "Bilateral analysis based false positive reduction for computer-aided mass detection," *Medical Physics*, vol. 34, no. 8, pp. 3334–3344, 2007.

[28] Z. Huo, M. L. Giger, C. J. Vyborny, D. E. Wolverton, R. A. Schmidt, and K. Doi, "Automated computerized classification of malignant and benign masses on digitized mammograms," *Academic Radiology*, vol. 5, no. 3, pp. 155–168, 1998.

[29] P. Delogu, M. E. Fantacci, P. Kasae, and A. Retico, "Characterization of mammographic masses using a gradient-based segmentation algorithm and a neural classifier," *Computers in Biology and Medicine*, vol. 37, no. 10, pp. 1479–1491, 2007.

[30] J. Shi, B. Sahiner, H. P. Chan et al., "Characterization of mammographic masses based on level set segmentation with new image features and patient information," *Medical Physics*, vol. 35, no. 1, pp. 280–290, 2008.

[31] H. Yoshida and J. Nappi, "Three-dimensional computer-aided diagnosis scheme for detection of colonic polyps," *IEEE Transactions on Medical Imaging*, vol. 20, no. 12, pp. 1261–1274, 2001.

[32] A. K. Jerebko, R. M. Summers, J. D. Malley, M. Franaszek, and C. D. Johnson, "Computer-assisted detection of colonic polyps with CT colonography using neural networks and binary classification trees," *Medical Physics*, vol. 30, no. 1, pp. 52–60, 2003.

[33] S. Wang, J. Yao, and R. M. Summers, "Improved classifier for computer-aided polyp detection in CT colonography by nonlinear dimensionality reduction," *Medical Physics*, vol. 35, no. 4, pp. 1377–1386, 2008.

[34] C. Muramatsu, Q. Li, R. A. Schmidt et al., "Determination of subjective similarity for pairs of masses and pairs of clustered microcalcifications on mammograms: comparison of similarity ranking scores and absolute similarity ratings," *Medical Physics*, vol. 34, no. 7, pp. 2890–2895, 2007.

[35] C. Muramatsu, Q. Li, R. Schmidt et al., "Experimental determination of subjective similarity for pairs of clustered microcalcifications on mammograms: observer study results," *Medical Physics*, vol. 33, no. 9, pp. 3460–3468, 2006.

[36] C. Muramatsu, Q. Li, K. Suzuki et al., "Investigation of psychophysical measure for evaluation of similar images for mammographic masses: preliminary results," *Medical Physics*, vol. 32, no. 7, pp. 2295–2304, 2005.

[37] H. Arimura, Q. Li, Y. Korogi et al., "Computerized detection of intracranial aneurysms for three-dimensional MR angiography: feature extraction of small protrusions based on a shape-based difference image technique," *Medical Physics*, vol. 33, no. 2, pp. 394–401, 2006.

[38] K. Suzuki, I. Horiba, N. Sugie, and M. Nanki, "Neural filter with selection of input features and its application to image quality improvement of medical image sequences," *IEICE Transactions on Information and Systems*, vol. E85-D, no. 10, pp. 1710–1718, 2002.

[39] K. Suzuki, I. Horiba, and N. Sugie, "Efficient approximation of neural filters for removing quantum noise from images," *IEEE Transactions on Signal Processing*, vol. 50, no. 7, pp. 1787–1799, 2002.

[40] K. Suzuki, I. Horiba, and N. Sugie, "Neural edge enhancer for supervised edge enhancement from noisy images," *IEEE Transactions on Pattern Analysis and Machine Intelligence*, vol. 25, no. 12, pp. 1582–1596, 2003.

[41] K. Suzuki, I. Horiba, N. Sugie, and M. Nanki, "Extraction of left ventricular contours from left ventriculograms by means of a neural edge detector," *IEEE Transactions on Medical Imaging*, vol. 23, no. 3, pp. 330–339, 2004.

[42] S. B. Lo, S. A. Lou, J. S. Lin, M. T. Freedman, M. V. Chien, and S. K. Mun, "Artificial convolution neural network techniques and applications for lung nodule detection," *IEEE*

Transactions on Medical Imaging, vol. 14, no. 4, pp. 711–718, 1995.

[43] S. C. B. Lo, H. P. Chan, J. S. Lin, H. Li, M. T. Freedman, and S. K. Mun, "Artificial convolution neural network for medical image pattern recognition," *Neural Networks*, vol. 8, no. 7-8, pp. 1201–1214, 1995.

[44] J. S. Lin, B. Shih-Chung, A. Hasegawa, M. T. Freedman, and S. K. Mun, "Reduction of false positives in lung nodule detection using a two-level neural classification," *IEEE Transactions on Medical Imaging*, vol. 15, no. 2, pp. 206–217, 1996.

[45] S. C. B. Lo, H. Li, Y. Wang, L. Kinnard, and M. T. Freedman, "A multiple circular path convolution neural network system for detection of mammographic masses," *IEEE Transactions on Medical Imaging*, vol. 21, no. 2, pp. 150–158, 2002.

[46] B. Sahiner, H. P. Chan, N. Petrick et al., "Classification of mass and normal breast tissue: a convolution neural network classifier with spatial domain and texture images," *IEEE Transactions on Medical Imaging*, vol. 15, no. 5, pp. 598–610, 1996.

[47] S. Lawrence, C. L. Giles, A. C. Tsoi, and A. D. Back, "Face recognition: a convolutional neural-network approach," *IEEE Transactions on Neural Networks*, vol. 8, no. 1, pp. 98–113, 1997.

[48] C. Neubauer, "Evaluation of convolutional neural networks for visual recognition," *IEEE Transactions on Neural Networks*, vol. 9, no. 4, pp. 685–696, 1998.

[49] D. Wei, R. M. Nishikawa, and K. Doi, "Application of texture analysis and shift-invariant artificial neural network to microcalcification cluster detection," *Radiology*, vol. 201, pp. 696–696, 1996.

[50] W. Zhang, K. Doi, M. L. Giger, R. M. Nishikawa, and R. A. Schmidt, "An improved shift-invariant artificial neural network for computerized detection of clustered microcalcifications in digital mammograms," *Medical Physics*, vol. 23, no. 4, pp. 595–601, 1996.

[51] W. Zhang, K. Doi, M. L. Giger, Y. Wu, R. M. Nishikawa, and R. A. Schmidt, "Computerized detection of clustered microcalcifications in digital mammograms using a shift-invariant artificial neural network," *Medical Physics*, vol. 21, no. 4, pp. 517–524, 1994.

[52] K. Suzuki, S. G. Armato III, F. Li, S. Sone, and K. Doi, "Massive training artificial neural network (MTANN) for reduction of false positives in computerized detection of lung nodules in low-dose computed tomography," *Medical Physics*, vol. 30, no. 7, pp. 1602–1617, 2003.

[53] K. Suzuki, H. Yoshida, J. Nappi, and A. H. Dachman, "Massive-training artificial neural network (MTANN) for reduction of false positives in computer-aided detection of polyps: suppression of rectal tubes," *Medical Physics*, vol. 33, no. 10, pp. 3814–3824, 2006.

[54] K. Suzuki, H. Abe, H. MacMahon, and K. Doi, "Image-processing technique for suppressing ribs in chest radiographs by means of massive training artificial neural network (MTANN)," *IEEE Transactions on Medical Imaging*, vol. 25, no. 4, pp. 406–416, 2006.

[55] S. Oda, K. Awai, K. Suzuki et al., "Performance of radiologists in detection of small pulmonary nodules on chest radiographs: effect of rib suppression with a massive-training artificial neural network," *American Journal of Roentgenology*, vol. 193, no. 5, pp. W397–W402, 2009.

[56] K. Suzuki, "A supervised "lesion-enhancement" filter by use of a massive-training artificial neural network (MTANN) in computer-aided diagnosis (CAD)," *Physics in Medicine and Biology*, vol. 54, no. 18, pp. S31–S45, 2009.

[57] K. Suzuki, J. Shiraishi, H. Abe, H. MacMahon, and K. Doi, "False-positive reduction in computer-aided diagnostic scheme for detecting nodules in chest radiographs by means of massive training artificial neural network," *Academic Radiology*, vol. 12, no. 2, pp. 191–201, 2005.

[58] K. Suzuki, F. Li, S. Sone, and K. Doi, "Computer-aided diagnostic scheme for distinction between benign and malignant nodules in thoracic low-dose CT by use of massive training artificial neural network," *IEEE Transactions on Medical Imaging*, vol. 24, no. 9, pp. 1138–1150, 2005.

[59] K. Suzuki, D. C. Rockey, and A. H. Dachman, "CT colonography: advanced computer-aided detection scheme utilizing MTANNs for detection of "missed" polyps in a multicenter clinical trial," *Medical Physics*, vol. 37, no. 1, pp. 12–21, 2010.

[60] K. Suzuki, H. Yoshida, J. Näppi, S. G. Armato III, and A. H. Dachman, "Mixture of expert 3D massive-training ANNs for reduction of multiple types of false positives in CAD for detection of polyps in CT colonography," *Medical Physics*, vol. 35, no. 2, pp. 694–703, 2008.

[61] K. Suzuki, J. Zhang, and J. Xu, "Massive-training artificial neural network coupled with laplacian-eigenfunction-based dimensionality reduction for computer-aided detection of polyps in CT colonography," *IEEE Transactions on Medical Imaging*, vol. 29, no. 11, Article ID 5491180, pp. 1907–1917, 2010.

[62] J. W. Xu and K. Suzuki, "Massive-training support vector regression and Gaussian process for false-positive reduction in computer-aided detection of polyps in CT colonography," *Medical Physics*, vol. 38, no. 4, pp. 1888–1902, 2011.

[63] F. Li, H. Arimura, K. Suzuki et al., "Computer-aided detection of peripheral lung cancers missed at CT: ROC analyses without and with localization," *Radiology*, vol. 237, no. 2, pp. 684–690, 2005.

[64] M. Loog and B. van Ginneken, "Segmentation of the posterior ribs in chest radiographs using iterated contextual pixel classification," *IEEE Transactions on Medical Imaging*, vol. 25, no. 5, pp. 602–611, 2006.

[65] M. Loog, B. van Ginneken, and A. M. R. Schilham, "Filter learning: application to suppression of bony structures from chest radiographs," *Medical Image Analysis*, vol. 10, no. 6, pp. 826–840, 2006.

[66] M. K. Ozkan, I. M. I. Sezan, and A. M. Tekalp, "Adaptive motion-compensated filtering of noisy image sequences," *IEEE Transactions on Circuits and Systems for Video Technology*, vol. 3, no. 4, pp. 277–290, 1993.

[67] J. Canny, "A computational approach to edge detection," *IEEE Transactions on Pattern Analysis and Machine Intelligence*, vol. 8, no. 6, pp. 679–698, 1986.

[68] D. Marr and E. Hildreth, "Theory of edge detection," *Proceedings of the Royal Society of London—Biological Sciences B*, vol. 207, no. 1167, pp. 187–217, 1980.

[69] M. H. Hueckel, "An operator which locates edges in digitized pictures," *Journal of Alternative and Complementary Medicine*, vol. 18, no. 1, pp. 113–125, 1971.

[70] K. Suzuki, H. Abe, F. Li, and K. Doi, "Suppression of the contrast of ribs in chest radiographs by means of massive training artificial neural network," in *Proceedings of the SPIE Medical Imaging (SPIE MI '04)*, pp. 1109–1119, San Diego, Calif, USA, February 2004.

[71] A. R. Barron, "Universal approximation bounds for superpositions of a sigmoidal function," *IEEE Transactions on Information Theory*, vol. 39, no. 3, pp. 930–945, 1993.

[72] K. Hornik, M. Stinchcombe, and H. White, "Multilayer feedforward networks are universal approximators," *Neural Networks*, vol. 2, no. 5, pp. 359–366, 1989.

[73] K. Suzuki, "Determining the receptive field of a neural filter," *Journal of Neural Engineering*, vol. 1, no. 4, pp. 228–237, 2004.

[74] K. Suzuki, I. Horiba, and N. Sugie, "A simple neural network pruning algorithm with application to filter synthesis," *Neural Processing Letters*, vol. 13, no. 1, pp. 43–53, 2001.

[75] Y. LeCun, B. Boser, J. S. Denker, D. Henderson, R. E. Howard, and W. Hubbard, "Backpropagation applied to handwritten zip code recognition," *Neural Computation*, vol. 1, no. 4, pp. 541–551, 1989.

[76] S. Deutsch, "A simplified version of Kunihiko Fukushima's neocognitron," *Biological Cybernetics*, vol. 42, no. 1, pp. 17–21, 1981.

[77] K. Fukushima, "Neocognitron capable of incremental learning," *Neural Networks*, vol. 17, no. 1, pp. 37–46, 2004.

[78] K. Fukushima, "Neocognitron: a self-organizing neural network model for a mechanism of pattern recognition unaffected by shift in position," *Biological Cybernetics*, vol. 36, no. 4, pp. 193–202, 1980.

[79] M. N. Gurcan, B. Sahiner, H. P. Chan, L. Hadjiiski, and N. Petrick, "Selection of an optimal neural network architecture for computer-aided detection of microcalcifications—comparison of automated optimization techniques," *Medical Physics*, vol. 28, no. 9, pp. 1937–1948, 2001.

[80] H. P. Chan, S. C. B. Lo, B. Sahiner, K. L. Lam, and M. A. Helvie, "Computer-aided detection of mammographic microcalcifications: pattern recognition with an artificial neural network," *Medical Physics*, vol. 22, no. 10, pp. 1555–1567, 1995.

[81] A. Hasegawa, K. Itoh, and Y. Ichioka, "Generalization of shift invariant neural networks: image processing of corneal endothelium," *Neural Networks*, vol. 9, no. 2, pp. 345–356, 1996.

[82] C. M. Bishop, "An example—character recognition," in *Neural Networks for Pattern Recognition*, C. M. Bishop, Ed., pp. 1–4, Oxford University Press, New York, NY, USA, 1995.

[83] D. F. Michaels, "Internal organization of classifier networks trained by backpropagation," in *Neural Networks in Vision and Pattern Recognition*, J. Skrzypek and W. Karplus, Eds., World Scientific, Singapore, 1992.

[84] C. M. Bishop, *Neural Networks for Pattern Recognition*, Oxford University Press, New York, NY, USA, 1995.

[85] I. Pitas, "Edge detection," in *Digital Image Processing Algorithms and Applications*, pp. 242–249, Wiley-Interscience, New York, NY, USA, 2000.

[86] C. J. Murray and A. D. Lopez, "Mortality by cause for eight regions of the world: global burden of disease study," *The Lancet*, vol. 349, no. 9061, pp. 1269–1276, 1997.

[87] G. E. Goodman, "Lung cancer. 1: prevention of lung cancer," *Thorax*, vol. 57, no. 11, pp. 994–999, 2002.

[88] J. H. Austin, B. M. Romney, and L. S. Goldsmith, "Missed bronchogenic carcinoma: radiographic findings in 27 patients with a potentially resectable lesion evident in retrospect," *Radiology*, vol. 182, no. 1, pp. 115–122, 1992.

[89] P. K. Shah, J. H. Austin, C. S. White et al., "Missed non-small cell lung cancer: radiographic findings of potentially resectable lesions evident only in retrospect," *Radiology*, vol. 226, no. 1, pp. 235–241, 2003.

[90] R. Glocker and W. Frohnmayer, "Uber die rontgenspektroskopische bestimmung des gewichtsanteiles eines elementes in gememgen und verbindungen," *Annalen der Physik*, vol. 76, pp. 369–395, 1925.

[91] B. Jacobson and R. S. Mackay, "Radiological contrast enhancing methods," *Advances in Biological and Medical Physics*, vol. 6, pp. 201–261, 1958.

[92] T. Ishigaki, S. Sakuma, and Y. Horikawa, "One-shot dual-energy subtraction imaging," *Radiology*, vol. 161, no. 1, pp. 271–273, 1986.

[93] T. Ishigaki, S. Sakuma, and M. Ikeda, "One-shot dual-energy subtraction chest imaging with computed radiography: clinical evaluation of film images," *Radiology*, vol. 168, no. 1, pp. 67–72, 1988.

[94] B. K. Stewart and H. K. Huang, "Single-exposure dual-energy computed radiography," *Medical Physics*, vol. 17, no. 5, pp. 866–875, 1990.

[95] D. L. Ergun, C. A. Mistretta, D. E. Brown et al., "Single-exposure dual-energy computed radiography: improved detection and processing," *Radiology*, vol. 174, no. 1, pp. 243–249, 1990.

[96] G. J. Whitman, L. T. Niklason, M. Pandit et al., "Dual-energy digital subtraction chest radiography: technical considerations," *Current Problems in Diagnostic Radiology*, vol. 31, no. 2, pp. 48–62, 2002.

[97] K. Doi, "Computer-aided diagnosis in medical imaging: historical review, current status and future potential," *Computerized Medical Imaging and Graphics*, vol. 31, no. 4-5, pp. 198–211, 2007.

[98] M. L. Giger, "Update on the potential role of CAD in radiologic interpretations: are we making progress?" *Academic Radiology*, vol. 12, no. 6, pp. 669–670, 2005.

[99] A. F. Frangi, W. J. Niessen, R. M. Hoogeveen, T. van Walsum, and M. A. Viergever, "Model-based quantitation of 3-D magnetic resonance angiographie images," *IEEE Transactions on Medical Imaging*, vol. 18, no. 10, pp. 946–956, 1999.

[100] L. He, Y. Chao, K. Suzuki, and K. Wu, "Fast connected-component labeling," *Pattern Recognition*, vol. 42, no. 9, pp. 1977–1987, 2009.

[101] L. He, Y. Chao, and K. Suzuki, "A run-based two-scan labeling algorithm," *IEEE Transactions on Image Processing*, vol. 17, no. 5, pp. 749–756, 2008.

[102] K. Suzuki, I. Horiba, and N. Sugie, "Linear-time connected-component labeling based on sequential local operations," *Computer Vision and Image Understanding*, vol. 89, no. 1, pp. 1–23, 2003.

[103] L. Boroczky, L. Zhao, and K. P. Lee, "Feature subset selection for improving the performance of false positive reduction in lung nodule CAD," *IEEE Transactions on Information Technology in Biomedicine*, vol. 10, no. 3, pp. 504–511, 2006.

[104] A. S. Roy, S. G. Armato III, A. Wilson, and K. Drukker, "Automated detection of lung nodules in CT scans: false-positive reduction with the radial-gradient index," *Medical Physics*, vol. 33, no. 4, pp. 1133–1140, 2006.

[105] Z. Hongbin, L. Zhengrong, J. P. Perry et al., "Increasing computer-aided detection specificity by projection features for CT colonography," *Medical Physics*, vol. 37, no. 4, pp. 1468–1481, 2010.

[106] G. Lordanescu and R. M. Summers, "Reduction of false positives on the rectal tube in computer-aided detection for CT colonography," *Medical Physics*, vol. 31, no. 10, pp. 2855–2862, 2004.

[107] J. Yao, J. Li, and R. M. Summers, "Employing topographical height map in colonic polyp measurement and false positive reduction," *Pattern Recognition*, vol. 42, no. 6, pp. 1029–1040, 2009.

[108] P. C. Bunch, J. F. Hamilton, G. K. Sanderson, and A. H. Simmons, "A free-response approach to the measurement and characterization of radiographic-observer performance," *Journal of Applied Photographic Engineering,* vol. 4, no. 4, pp. 166–171, 1978.